JOURNAL OF PROPULSION AND POWER
Vol. 9, No. 3, May–June 1993

# Efficient Hybrid Scheme for the Analysis of Counter-Rotating Propellers

R. Srivastava* and Lakshmi N. Sankar†
*Georgia Institute of Technology, Atlanta, Georgia 30332*

**An efficient solution procedure has been developed for analyzing inviscid unsteady flow past counter-rotation propellers. This scheme is first-order accurate in time and second-order accurate in space. The spatial accuracy can be extended to fourth-order in the axial direction. The solution procedure has been applied to a two-bladed SR-7 single-rotor propeller and to a GE F7/A7 counter-rotating propeller. The pressure coefficients and the global quantities, power and thrust, show good correlation with experimental measurements.**

## Introduction

MODERN high-speed propellers are designed to delay the compressibility losses and to extend the high efficiency of a propeller to relatively high-cruise Mach numbers. This is accomplished by sweeping the blade backwards and using thinner airfoils on the outboard section of the blade. In addition, low-aspect ratio blades are used. This, combined with high-tip Mach number, leads to high-blade twist and high-disk loading. The requirement of high-disk loading further dictates a large number of blades per propeller. However, as the blades are highly loaded, loss in efficiency due to swirl becomes important. By recovering the swirl losses, the efficiency can be further increased by 4–5%. This can be done either by using stationary guide vanes, as done in turbomachinery, or by another row of blades rotating in the opposite direction. Using thinner airfoil sections, on the one hand, helps in delaying the drag divergence, but on the other hand, it leads to flexible blades. Due to the flexibility, some of the advanced propeller blades have either fluttered or undergone large amplitude oscillations in wind-tunnel tests.[1] As these propellers have high fuel saving potential, numerical capabilities need to be developed to predict the catastrophic aeroelastic instabilities for these advanced propellers.

Several numerical techniques varying in complexity, from simple Goldstein-type strip analysis to analyses that solve the Euler and Navier-Stokes equations,[2–12] have been applied to single-rotor propellers for aerodynamic analysis. Several researchers have extended these earlier works to aerodynamic analysis of counter-rotating propellers. Celestina et al.[13] have solved the steady Euler equations around a counter-rotating configuration using an average passage scheme. Whitfield et al.[10] solved the unsteady Euler equations around the counter-rotating configuration using a finite volume scheme. The scheme was later modified in Ref. 14 to allow arbitrary time step. Kobayakawa and Nakao[15] have solved the flowfield around a counter-rotating propeller by recasting the unsteady Euler equations in a weak conservation form. These equations are discretized using finite difference formulas, then solved using an alternating direction implicit (ADI) scheme. The above-mentioned schemes are either restricted to steady flow calculations or are computationally intensive, therefore, they are not suitable for aeroelastic calculations.

## Objectives

The primary objective of the present research is to develop an efficient method for predicting the aeroelastic characteristics of a counter-rotating propeller. As a first step to such aeroelastic applications, the efficient hybrid method developed in Ref 12 for single-rotor propellers, has been modified for aerodynamic analysis of unducted counter-rotating propellers. The method is used to compute the steady airloads and performance characteristics of the SR-7 single-rotor propeller, and the GE F7/A7 unducted counter-rotating propeller.

## Formulation

### Solution Procedure

The Euler equations, in conservation form, in a Cartesian coordinate system can be written as

$$(\hat{q})_t + (\hat{E})_x + (\hat{F})_y + (\hat{G})_z = 0 \qquad (1)$$

where $\hat{q}$ is the vector containing conserved flow properties. $\hat{E}$, $\hat{F}$, and $\hat{G}$ are the nonlinear flux vectors which are functions of the vector $\hat{q}$, the subscripts denote the partial derivative of the vector. To simplify treatment of arbitrary geometries, the Euler equations in Eq. (1) are transformed and recast in a generalized coordinate system. The transformed equations are then solved using a semi-implicit hybrid algorithm similar to the scheme by Rizk and Chaussee.[16] In the present scheme, in order to decrease the computational time, flux terms in two directions are treated implicitly, while the radial direction flux terms are treated semi-implicitly. The derivatives in the radial direction are obtained using the latest available values of the flow variables. Firist-order accurate implicit Euler rule is used for time derivative, and second-order accurate central difference is used for spatial derivatives. Second/fourth difference explicit dissipation and a second-order implicit dissipation is used to make the scheme stable and to reduce the high-frequency errors. This leads to a block pentadiagonal system of equations coupling the nonlinear fluxes being treated implicitly. As in the Beam-Warming algorithm,[17] these fluxes are linearized about their values at the previous time level, resulting in a block pentadiagonal system of equations for the changes in the flow properties. This pentadiagonal system is approximately factored into two-block tridiagonal system of equations, and inverted using Thomas algorithm.[12]

The present scheme, for counter-rotating propellers, is an extension of the solution procedure developed in Ref. 12 for analyzing single-rotor propellers. The spatial accuracy of the

Received Nov. 11, 1990; presented as Paper 91-0703 at the AIAA 29th Aerospace Sciences Meeting, Reno, NV, Jan. 7–10, 1991; revision received Nov. 6, 1992; accepted for publication Nov. 27, 1992.


*Postdoctoral Fellow, School of Aerospace Engineering; currently Resident Research Associate, NASA Lewis Research Center, Cleveland, Ohio 44135. Member AIAA.
†Professor, School of Aerospace Engineering. Member AIAA.

original hybrid scheme of Ref. 12 can be increased to fourth-order in any of one or more directions, using the Pade approximation, without significantly increasing the computer requirement. The only additional work required is to invert a tridiagonal matrix for each grid line in the direction of the higher accuracy. Interested readers may refer to Ref. 18 for a detailed description of the Pade approximation.

The efficiency of the scheme is derived from the fact that the hybrid procedure inherently requires less computer memory (approximately half of fully implicit schemes) and less CPU time, as only two-block tridiagonal matrices need to be inverted, as opposed to three for fully implicit schemes. The two inversions of the block tridiagonal matrices are in the two implicit directions. The memory requirement is reduced because only two time levels of information need to be stored at any given time, only one of which needs to be three-dimensional.

Because two rows of blades in relative motion must be analyzed, the flowfield is solved using multiblock grid technique, with only one grid and its solution being in the core memory at any given time. The interface boundaries, along with other boundaries, are updated explicitly after all the interior points have been updated.

#### Initial and Boundary Conditions

The Euler equations are solved by marching in time. This requires an initial condition for the flowfield. The initial conditions may be important to rate of convergence and convergence itself. Hence, it is important to use a reasonable initial condition. An easily implemented initial condition used here is to set the whole flowfield at its freestream value.

In the present analysis, the flow variables at the boundaries are updated explicitly after the governing equations have been solved for the interior flowfield. On the solid surfaces of blade and nacelle, the no-penetration condition is applied as

$$V_b \cdot \boldsymbol{n} = 0 \tag{2}$$

where $V_b$ is the relative velocity vector between fluid and solid at the surface, and $\boldsymbol{n}$ is the outward unit vector normal to the surface. The tangential velocity components, pressure and density, are extrapolated from the interior of the domain.

For steady-state calculations, all disturbances from the solid surface must propagate to infinity. On the subsonic inflow boundary, one characteristic should be allowed to escape, thus, one characteristic quantity is extrapolated from the interior of the domain and the other four quantities are fixed to that of the freestream, as discussed in Ref. 10. However, because the characteristic boundary conditions are based on a locally one-dimensional steady flow approximation, they may not be suitable for the unsteady inflow such as gusts. Hence, for unsteady subsonic inflow, a reasonable approximation is to extrapolate one fluid property from the interior of the domain and to fix the other four fluid properties to that of the freestream. Therefore, for unsteady subsonic inflow, density is extrapolated, and the three components of momentum and energy are fixed at the freestream value. For a supersonic inflow boundary, all quantities are fixed to that of the freestream. In the present study, as only steady inflows are considered, the characteristics are used to update the inflow boundary.

At the subsonic outflow boundary, four characteristics should escape, therefore, four fluid properties are extrapolated from the interior of the domain using the one-dimensional characteristics approximation as discussed in Ref. 10. The static pressure is obtained by solving the simple radial equilibrium equation[19]

$$\frac{\partial p}{\partial r} = \frac{\rho v_\theta^2}{r} \tag{3}$$

where $p$ is the pressure, $\rho$ is the density, $v_\theta$ is the tangential velocity, and $r$ is the radius. For supersonic outflow, all characteristics should escape, hence, all quantities are extrapolated from inside the flow domain.

#### Block Interface Boundary

It is neither efficient nor practical to solve all the blade passages simultaneously, therefore, one blade passage is handled at a time. This introduces additional boundaries in the computation. Across these boundaries, all the variables must be continuous, except on solid boundaries. The boundary condition for these boundaries depends on the type of flow being solved. Axisymmetry would require periodicity at the fluid block interface boundaries. Periodicity will require that all the fluid boundaries between the blade passages have the same fluid properties.

For an asymmetric flow (e.g., propeller at an angle of attack), periodicity on these boundaries does not exist. Also, in order to obtain the solution for such a problem, the flowfield in all blade passages should be solved. This is done by advancing the solution of each block by one time step, one block at a time. In this case again, the boundaries are updated explicitly, after the interior points have been updated. This is done by averaging the conserved flow variables from the nodes on each side of the boundary from the adjoining blocks.

#### Row Interface Boundary

To simplify the solution procedure, the domain of counter-rotating blades is divided into two sets of blocks associated with each blade row. This creates an additional fluid boundary. As is done to the rest of the boundaries, this boundary is also updated explicitly after the interior of the computational domain has been updated. The flow properties on this boundary are updated as the average of the values of adjacent constant axial planes. However, as the two blocks are rotating in the opposite direction, the grid lines do not always align.

To carry out the averaging process, the solution needs to be known for the 360-deg ring at the axial location adjacent to the row interface boundary. For an asymmetric flowfield, this information is automatically available, as all the blade passages are solved. For an axisymmetric flowfield, where it may be sufficient to solve only one blade passage for each blade row, this information is obtained by imaging the block data to obtain flow properties for the 360-deg ring.

A schematic diagram of the grid at the interface boundary for a constant $\eta$ plane is shown in Fig. 1. The $I = IMAX$ plane for the front blade row and $I = 1$ plane of the aft blade row form the interface boundary. The interface boundary of the aft blade row is updated first, one grid point at a time.

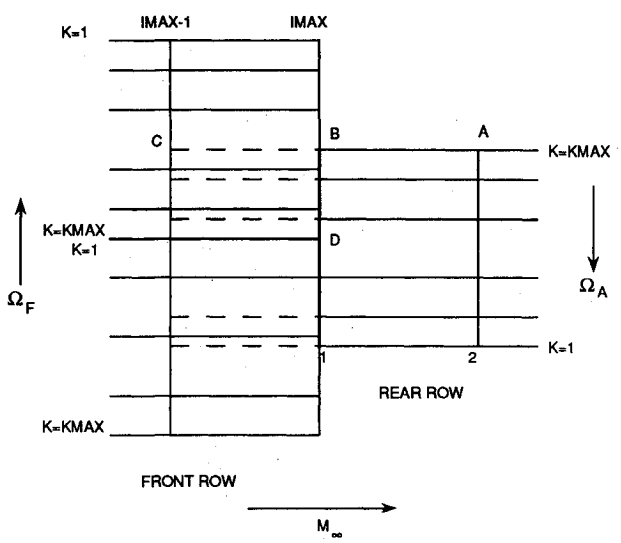


**Fig. 1 Row-interface boundaries.**

In order to update the flow properties at the node B (refer to Fig. 1), the grid line AB is extended until it intersects the plane $I = IMAX - 1$ of the front row at point C. The flow properties are then obtained at point C by interpolating from the flow properties of the $IMAX - 1$ plane using a Lagrangian polynominal fit. The node B is then updated by taking the average of the values at node A and point C. This is repeated for all the nodes associated with $I = 1$ plane of the aft row.

Again, for an axisymmetric flowfield, this is done for only one block and the solution is imaged. For an asymmetric flowfield, the process is repeated for all the nodes for all blades passages. The boundary $I = IMAX$ of the front row is then updated by simply interpolating flow variables from the boundary $I = 1$ of the aft row. The only requirement in this process, in order to minimize the error, is that the constant radial-surfaces from both the rows, at the interface boundary, be at the same radial distance.

It should be noted, however, that the present method of interpolation based on averaging the flow properties across the fluid boundaries is not conservative. However, since the flight conditions to be encountered by the propeller is at best, high subsonic, the nonconservativeness was not considered to be a serious deficiency. Also, as the row interface boundary will see the unsteady wake of the front blade row, updating the boundaries using the characteristics was not considered. The advantage, however, with the present scheme is that it provides a simple technique to obtain unsteady flow solution without restricting time steps or requiring grid deformations across stationary or relatively moving commonface fluid boundaries.

## Results and Discussion

### Single-Rotor Propellor Studies

The hybrid numerical scheme discussed in the previous section was first applied to a single-rotor propeller in Ref. 12, and has been validated for several flight conditions in Ref. 18. In Fig. 2, the pressure coefficient for a two-bladed SR7 propeller is compared with experimental data[20] for different span locations, for freestream Mach number of 0.2, advance ratio of 0.881, and setting angle of 30.4 deg. These calculations were carried out using the fourth-order scheme along the streamwise direction on a 100 × 22 × 35 grid, with 46 × 15 grid points on each of the blade surfaces. The effect of grid spacing in the normal direction is also shown in this figure. Three different normal spacings have been used, however, the number of grid points have been kept the same. As can be seen, the smaller the normal spacing, the better the comparison with experimental data, especially the suction peak. The agreement between pressure coefficients is good all along the span of the blade.

The error for larger normal spacing is greater for the inboard stations where the airfoil sections are thicker and the pressure suction peaks are higher. Using a second-order accurate scheme, with a relatively coarse grid, leads to wiggles near the leading edge.[18] These wiggles can be reduced using the fourth-order scheme along the streamwise direction. A leading-edge vortex exists for this flight condition, as can be observed from the plot of measured pressure coefficients. The vortex location moves down the chord from hub to tip, and is in the midchord, near the tip region. As a leading-edge vortex is a purely viscous phenomena, it may not be possible for an Euler analysis to properly capture it.

### Counter-Rotation Propeller Studies

The scheme has been applied here to a GE F7/A7 counter-rotating propeller model operating at a freestream Mach number of 0.71. This propeller has eight blades in each blade row. Both blade rows operate at the same advance ratio. The blade setting angles reported in experiments[21] were 58.5 deg for the front blade row and 55.7 deg for the aft blade row. In the analysis, the setting angles were changed to 58.3 deg for the front row and 54.4 deg for the aft row, to match the individual row power coefficient at the advance ratio of 3.0. The setting angles have been adjusted to account for the inaccuracies and tolerances of the measurements, inability to properly account for the blade deformations under loading, and the fact that viscous effects are neglected in the present calculations. A detailed explanation has been provided in Ref. 18. These setting angles were then used for all other advance ratios. Again, as in the case of single-rotor propeller, a body fitted H-O grid was used for calculating the flowfield around the counter-rotating propeller. A typical wire frame grid is shown in Fig. 3. In the present calculations, for each blade passage a 80 × 22 × 15 grid was used with 36 × 15 grid points on each blade surface. It must be acknowledged that the present grid is fairly coarse and is inadequate to model the nose of the hub and its influence properly.

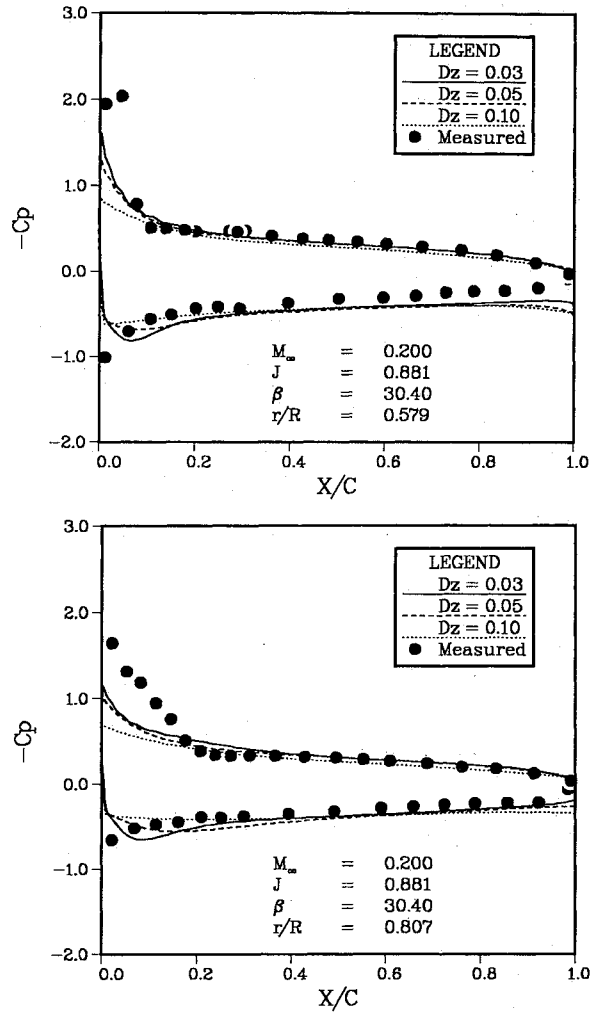


**Fig. 2 Comparison of chordwise variation of pressure coefficient at constant span locations for a SR7L 2-bladed propeller operating at $M_\infty = 0.2$.**

In general, in order to model the influence of adjacent blades (cascade effect), the entire propeller with all the blades (passages) needs to be solved. However, for an axisymmetric flowfield with same number of blades in both the rows (considered here), all blade passages of one blade row can be assumed to be identical. Hence, only one blade passage for each blade row is solved, enforcing the conditions of symmetry. Even though the flowfield is axisymmetric, it is unsteady, being periodic through the blade passages for each row. Therefore, the power coefficient was monitored, rather than the residuals, to determine the convergence of the solution. For the advance ratio of 3.0 (both the blade rows are operating at the same advance ratio), the variation of power coefficient is plotted vs rotation angle of the front blade row

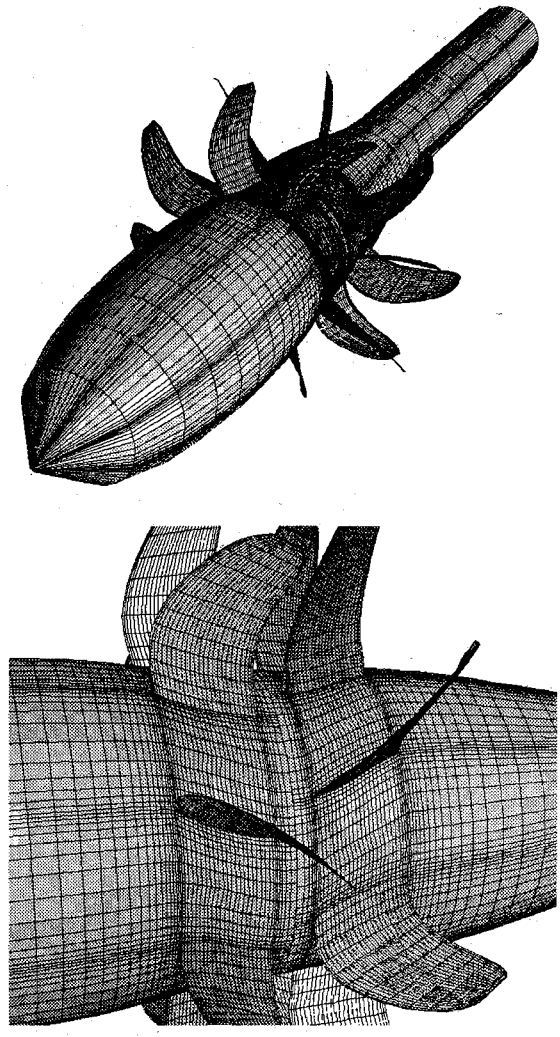

Fig. 3 Typical wire frame grid for the GE F7/A7 counter-rotating propeller.

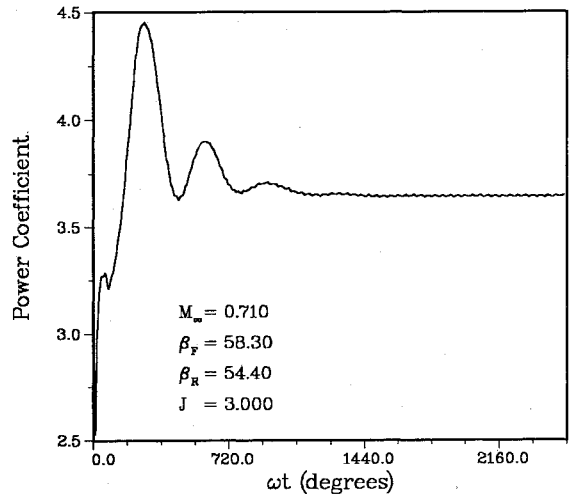


Fig. 4 Power coefficient convergence trend for GE F7/A7 counter-rotating propeller.

in Fig. 4. It takes approximately three and a half revolutions for the mean value of the unsteady power coefficient to reach convergence. In Fig. 5, the variation of power coefficient with rotation angle for one revolution of the front blade row is plotted, after the power coefficient has converged. As can be seen, the mean value and the amplitude of oscillation remain constant with time. The peak-to-peak variation of power coefficient is approximately ½% of the mean value. These oscillations are due to the fact that the relative blade positions of the two blade rows vary with time. Note, that even though the advance ratio is the same for both blade rows, the diameter of the aft row is slightly smaller than the front blade row, therefore, the aft blade row is rotating at a higher rpm than the front blade row. For this reason, the power coefficient oscillation for one revolution of front blade row is slightly more than 16 cycles.

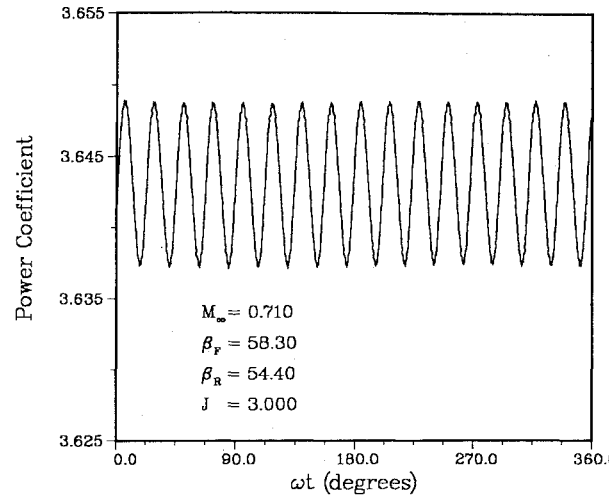


Fig. 5 Power coefficient variation of GE F7/A7 counter-rotating propeller for one revolution of the front row.

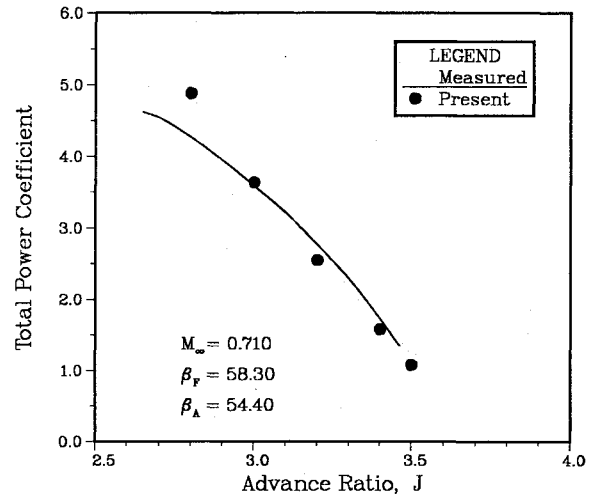


Fig. 6 Comparison of total power coefficient for GE F7/A7 counter-rotating propeller.

The time-averaged steady power coefficients and the thrust coefficients are compared with experimental data[21] in Figs. 6–8, and 9–11, respectively. The total power and thrust coefficients (Figs. 6 and 9) are overpredicted at the lower advance ratio of 2.8, whereas they compare well with experiment for higher advance ratios. The individual blade row power coefficients (Figs. 7 and 8) exhibit the same trend. The thrust coefficient for the front blade row (Fig. 10) is consistently overpredicted for all advance ratios, whereas the aft row thrust coefficient (Fig. 11) is well-predicted for all advance ratios, except at 2.8. In general, the aft row performance characteristics are well-predicted. In Fig. 12, the variation of torque ratio (aft rotor:front rotor) with advance ratio is compared. The torque ratio is well-predicted for all advance ratios.

From these figures it can be seen that the predictions of the global performance quantities compare well with experimental data. At the lower advance ratios, the blades are

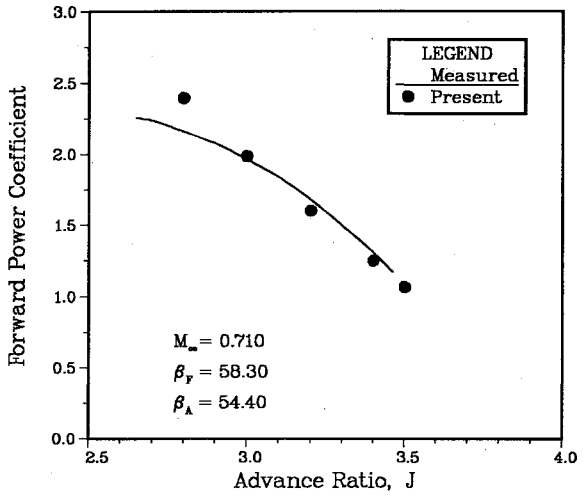


**Fig. 7 Comparison of forward rotor power coefficient for GE F7/A7 counter-rotating propeller.**

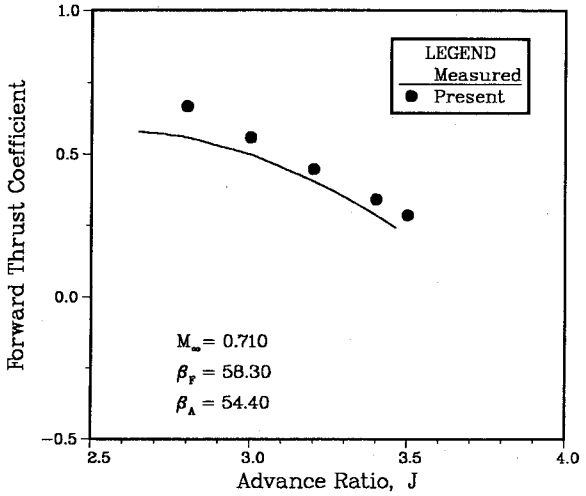


**Fig. 10 Comparison of forward rotor thrust coefficient for GE F7/A7 counter-rotating propeller.**

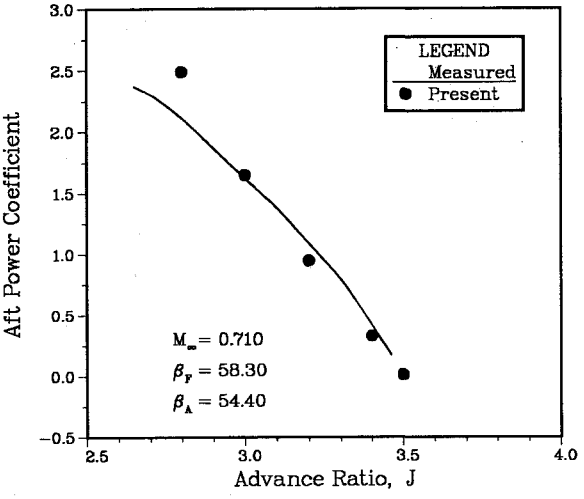


**Fig. 8 Comparison of aft rotor power coefficient for GE F7/A7 counter-rotating propeller.**

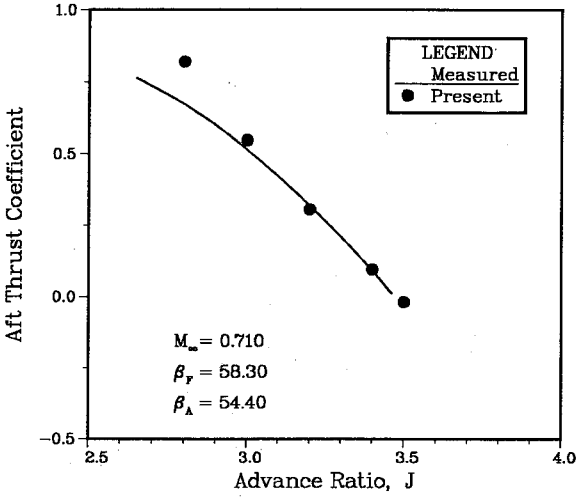


**Fig. 11 Comparison of aft rotor thrust coefficient for GE F7/A7 counter-rotating propeller.**

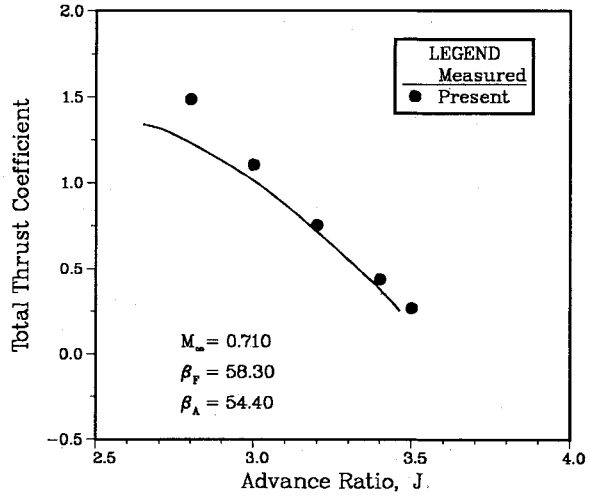


**Fig. 9 Comparison of total thrust coefficient for GE F7/A7 counter-rotating propeller.**

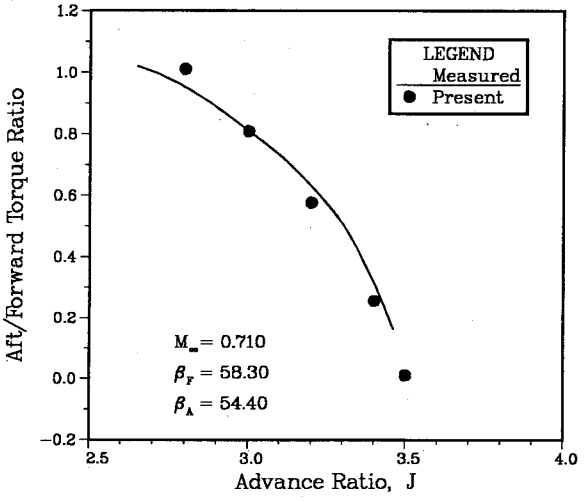


**Fig. 12 Comparison of aft rotor:forward rotor torque ratio for GE F7/A7 counter-rotating propeller.**

heavily loaded. This causes the blade to deflect more during operation. It is not possible to account for such deflections in a purely aerodynamic analysis of the present study. Also, the Euler calculations tend to overpredict the shock strength, which leads to higher wave drag. Furthermore, the present inviscid analysis cannot account for complex shock-wave and boundary-layer interaction, flow separation, and leading-edge vortices. Any or all of the above factors may have contributed to the overprediction of the performance parameters at the lower advance ratio.

In Figs. 13–16, the pressure and density contours are plotted at two radial locations, near the centerbody and near the midspan. The front rotor is rotating in a counterclockwise direction, and the aft rotor is rotating in the clockwise direc-

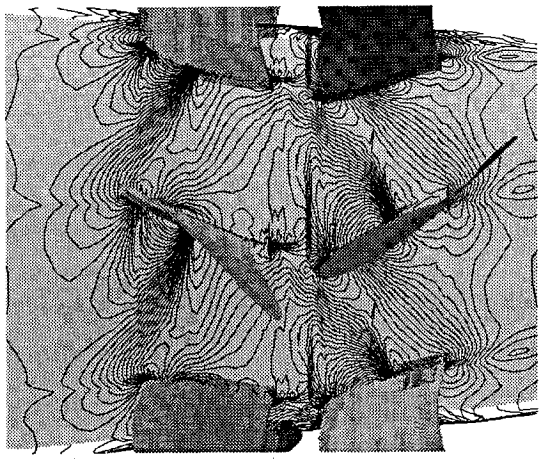

**Fig. 13 Density contours at constant $\eta$ plane on nacelle for GE F7/A7 counter-rotating propeller operating at $M_\infty = 0.71$, $J = 3.0$, $\beta_F = 58.3$, $\beta_A = 54.4$.**

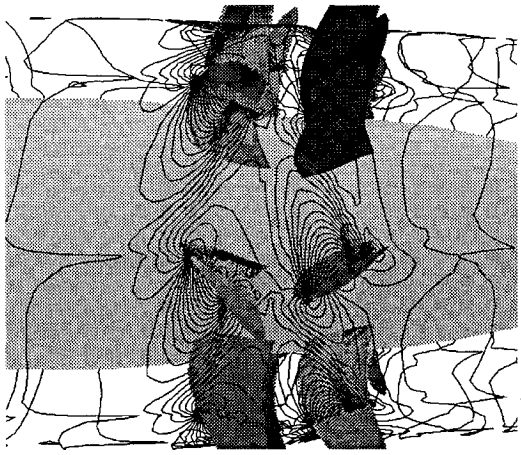

**Fig. 14 Density contours at constant $\eta$ plane near midspan for GE F7/A7 counter-rotating propeller operating at $M_\infty = 0.71$, $J = 3.0$, $\beta_F = 58.3$, $\beta_A = 54.4$.**

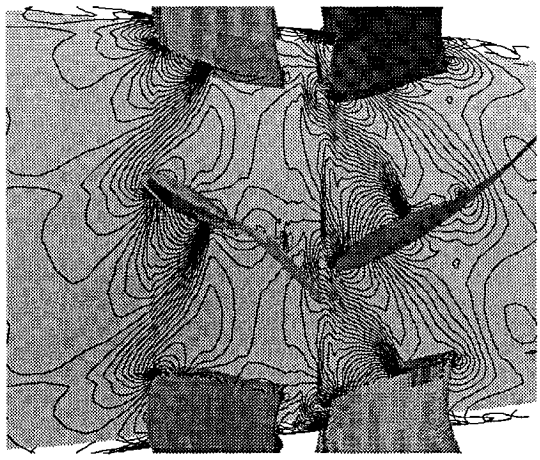

**Fig. 15 Pressure contours at constant $\eta$ plane on nacelle for GE F7/A7 counter-rotating propeller operating at $M_\infty = 0.71$, $J = 3.0$, $\beta_F = 58.3$, $\beta_A = 54.4$.**

tion, as viewed from the front of the propeller (left side of the figure). The freestream is moving from left to right, with a relative Mach number of 0.71, and the advance ratio for both the blade rows is 3.0. The pressure and the density contours shown in these figures, are continuous and smoothly varying between the blade rows and across the row interface boundary. This shows that the treatment of the interface boundary, as discussed earlier, does not introduce any significant error. The interface boundary lies exactly halfway between the two blade rows. Similar behavior was observed for other flow properties along the entire span of the blade. These figures also show that a strong shock exists on the suction surface on the blades of both the blade rows. The shock does not extend from blade-to-blade, and its strength reduces, away from the centerbody. The shock also moves along the chord, towards the trailing edge, away from the centerbody.

**Fig. 16 Pressure contours at constant $\eta$ plane near midspan for counter-rotating propeller operating at $M_\infty = 0.71$, $J = 3.0$, $\beta_F = 58.3$ $\beta_A = 54.4$.**

All of the above computations were performed on the CRAY Y-MP computer at NASA Lewis Research Center. For a grid size of 80 × 22 × 15, used for one blade passage of one blade row of the counter-rotating propeller, the total memory and CPU time required per time step were 1.8 MW and 1.594 s, respectively.

## Concluding Remarks

A solution procedure for computing inviscid flow past counter-rotating propellers has been developed. This procedure is computationally efficient and may be used to study the aerodynamic performance characteristics of modern propellers.

The pressure coefficients obtained by the present scheme compare well with experimental data for the single-rotor propeller. The calculations also show that a sufficiently fine grid must be used in the normal direction to capture the large suction peaks at the leading-edge regions of propeller blades. The study of the counter-rotating propeller showed that the present scheme of handling the row interface boundary does not impose any restrictions on the time step. Furthermore, it does not require any complex interpolation or grid deformation. The error introduced does not appear to be significant. The global quantities, power and thrust, and their variation with advance ratio, compare well with experimental measurement for counter-rotating propeller.

## Acknowledgments

This work has been carried out under NASA Grant NAG3-730 from NASA Lewis Research Center in Cleveland, Ohio. George L. Stefko is the grant monitor.

## References

[1]Mehmed, O., and Kaza, K. R. V., "Experimental Classical Flutter Results of a Composite Advanced Turboprop Model," NASA TM-88792, July 1986.

[2]Goldstein, S., "On the Vortex Theory of Screw Propellers," *Royal Society Proceedings*, Vol. 123, No. 792, 1929, pp. 440–465.

[3]Sullivan, J. P., "The Effect of Blade Sweep on Propeller Performance," AIAA Paper 77-176, June 1977.

[4]Egolf, T. A., Anderson, O. L., Edwards, D. E., and Landgrebe,

A. J., "An Analysis for High Speed Propeller-Nacelle Aerodynamic Performance Prediction; Volume 1, Theory and Initial Application and Volume 2, User's Manual for the Computer Program," United Technologies Research Center, R79-912949-19, East Hartford, CT, June 1979.

[5]Hanson, D. B., "Compressible Lifting Surface Theory for Propeller Performance Calculation," *Journal of Aircraft*, Vol. 22, No. 1, 1985, pp. 19–27.

[6]Williams, M. H., and Hwang, C., "Three Dimensional Unsteady Aerodynamics and Aeroelastic Response of Advanced Turboprops," AIAA Paper 86-0846, May 1986.

[7]Jou, W. H., "Finite Volume Calculation of the Three-Dimensional Flow Around a Propeller," AIAA Paper 82-0957, June 1982.

[8]Jameson, A., and Caughy, D. A., "A Finite Volume Method for Transonic Potential Flow Calculations," AIAA Paper 77-635, June 1977.

[9]Chaussee, D. S., "Computation of Three-Dimensional Flow Through Prop Fans," Nielsen Engineering and Research TR-199, Mountain View, CA, June 1979.

[10]Whitfield, D. L., Swafford, T. W., Janus, J. M., Mulac, R. A., and Belk, D. M., "Three-Dimensional Unsteady Euler Solutions for Propfans and Counter-Rotating Propfans in Transonic Flow," AIAA Paper 87-1197, June 1987.

[11]Matsuo, Y., Arakawa, C., Saito, S., and Kobayashi, H., "Navier-Stokes Computations for Flowfield of an Advanced Turboprop," AIAA Paper 88-3094, July 1988.

[12]Srivastava, R., Sankar, N. L., Reddy, T. S. R., and Huff, D. L., "Application of an Efficient Hybrid Scheme for Aeroelastic Analysis of Advanced Propellers," *Journal of Propulsion and Power* (to be published).

[13]Celestina, M. L., Mulac, R. A., and Adamczyk, J. J., "A Numerical Simulation of the Inviscid Flow Through a Counter-Rotating Propeller," NASA TM-87200, June 1986.

[14]Janus, J. M., and Whitfield, D. L., "Counterrotating Prop-Fan Simulations Which Feature a Relative Multiblock Grid Decomposition Enabling Arbitrary Time Steps," AIAA Paper 90-0687, Jan. 1990.

[15]Kobayakawa, M., and Nakao, M., "Numerical Solutions for the Flowfield Around a Counter-Rotating Propeller," *Journal of Aircraft*, Vol. 26, No. 5, 1989, pp. 417–422.

[16]Rizk, Y. M., and Chaussee, D. S., "Three-Dimensional Viscous-Flow Computations Using a Directionally Hybrid Implicit-Explicit Procedure," AIAA Paper 83-1910, July 1983.

[17]Beam, R. M., and Warming, R. F., "An Implicit Factored Scheme for the Compressible Navier-Stokes Equations," *AIAA Journal*, Vol. 16, No. 4, 1978, pp. 393–402.

[18]Srivastava, R., "An Efficient Hybrid Scheme for the Solution of Rotational Flow Around Advanced Propellers," Ph.D. Dissertation, Georgia Inst. of Technology, Atlanta, GA, 1990.

[19]Horlock, J. H., *Axial Flow Turbines—Fluid Mechanics and Thermodynamics*, Robert E. Krieger Publishing, Malabar, FL, 1982, pp. 11–13, 148.

[20]Bushnell, P., "Measurement of the Steady Surface Pressure Distribution on a Single Rotation Large Scale Advanced Prop-Fan Blade at Mach Numbers from 0.03 to 0.78," NASA CR 182124, July 1988.

[21]Jeraki, R. J., and Rose, G. E., "Effects of Mach Number, Loading, and Blade Angle on High-Speed Performance of the F7/A7 Highly Loaded Counterrotation Propeller," NASA TP 2927, 1991.